Supplementary Information

Identification of physical origin behind disorder, heterogeneity, and reconstruction and their correlation with Photoluminescence lifetime in hybrid perovskite thin film

Taame Abraha Berhe[1,#], Ju-Hsiang Cheng[2,#], Wei-Nien Su[1,*], Chun-Jern Pan[2], Meng-Che Tsai[2], Hung-Ming Chen[2], Zhenyu Yang[3], Hairen Tan[3], Ching-Hsiang Chen[2], Min-Hsin Yeh[2], Andebet Gedamu Tamirat[2], Shin-Fu Huang[2], Liang-Yih Chen[2], Jyh-Fu Lee[4],Yen-Fa Liao[4], Edward H. Sargent[3,*], Hongjie Dai[5] and Bing-Joe Hwang[2,4,*]

[1]*NanoElectrochemistry Laboratory, Graduate Institute of Applied Science and Technology, National Taiwan University of Science and Technology, Taipei 106, Taiwan*
[2]*NanoElectrochemistry Laboratory, Department of Chemical Engineering, National Taiwan University of Science and Technology, Taipei 106, Taiwan*
[3]*Department of Electrical and Computer Engineering, University of Toronto, 35 St George Street, Toronto, Ontario M5S 1A4, Canada*
[4]*National Synchrotron Radiation Research Center, Hsin-Chu 30076, Taiwan*
[5]*Department of Chemistry, Stanford University, Stanford, CA, California 94305-4401, USA*
**Corresponding Authors: E-mail: bjh@mail.ntust.edu.tw (B. J. Hwang), wsu@mail.ntust.edu.tw (W. N. Su) and ted.sargent@utoronto.ca (Edward H. Sargent)*

[#]*These authors have equal contribution in this work*

Characterization techniques

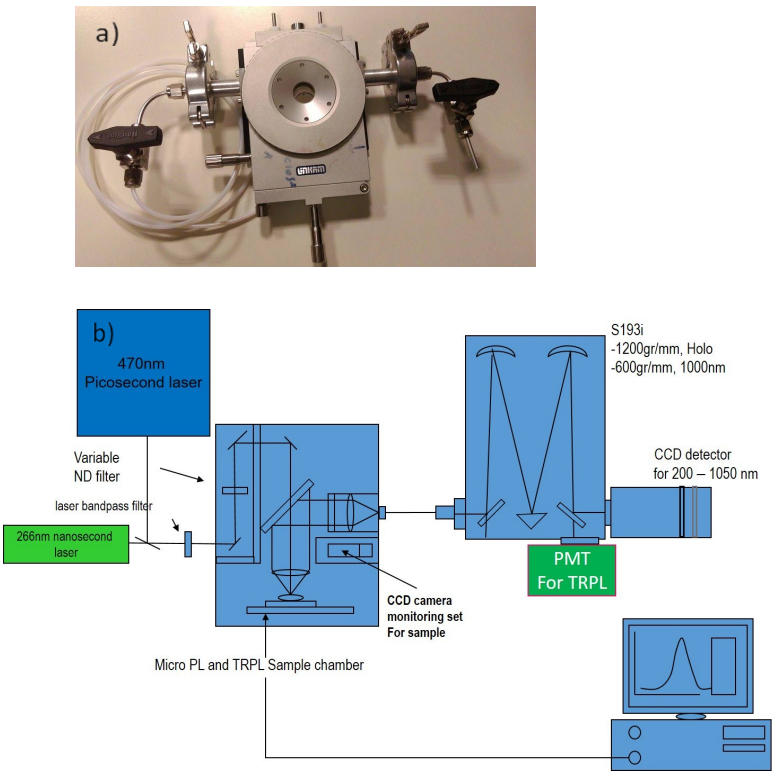

Fig. S1. System for lifetime measurement: (a) *In-situ* device (sample stage) made of quartz glass to avoid air and moisture contact during Raman and decay time measurements and, (b) experimental setup (layout) for PL (266 nm) and TRPL measurement (470 nm) as well as emission wavelength is 765 nm.

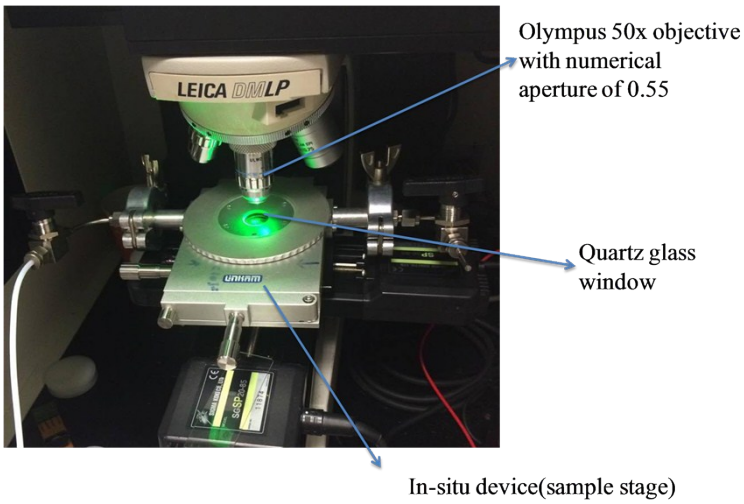

Fig. S2. Experimental setup for *in-situ* micro Raman spectroscopy measurement.

Differential scanning calorimeter (DSC)

DSC was conducted on a Q10 V9.9 Build 303 calorimeter (TA Instruments) at a rate of 5°C min^{-1} over a temperature range from 30°C to 200°C under nitrogen gas flow. 6 mg of $CH_3NH_3PbI_3$ fine-grained powder was used during DSC experiment. Note that the samples have been exposed to air during measurements.

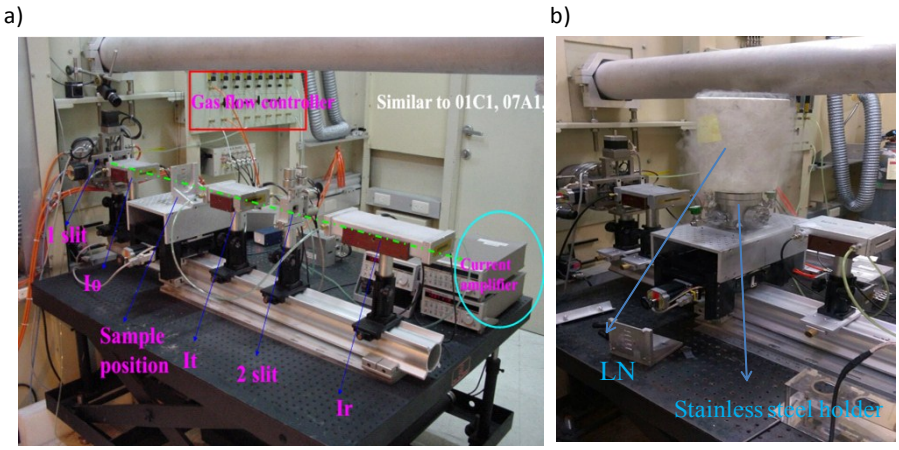

Fig. S3 *In-situ* X-ray absorption measurement: (a) General experimental layout for (17C1) and (b) stainless steel sample holder position for x-ray absorption measurement for different temperature. Note that the setup for XAS measurement, the ion chambers, the I_0, I_t and I_r are used to detect the x-ray signal. The sample is positioned in between the I_0 and I_t.

X-ray Absorption Spectroscopy Data Analysis

Standard procedures were followed to analyze the EXAFS data[1] using Athena software[2]: Firstly, the raw absorption spectrum in the pre-edge region was fitted to a straight line. The background was fitted with a cubic spline. The EXAFS function χ was obtained by subtracting the post-edge background from the overall absorption and then normalized with respect to the edge jump step. The normalized $\chi(E)$ was transformed from energy space to k-space, where k is the photoelectron wave vector. The $\chi(k)$ data were multiplied by k^3 to compensate for the damping of EXAFS oscillations in the high k-region. Subsequently, k^3-weighted $\chi(k)$ data in the k-space ranging from 2.7 to 12 $Å^{-1}$ for the Pb L_3-edge were Fourier transformed (FT) to r-space to separate the EXAFS contributions from the different coordination shells. A nonlinear least squares algorithm was applied to the curve fitting of an EXAFS in the r-space between 1.7 to 3.4 Å (without phase correction) for Pb. Atomic information is derived from the normalized absorption fine structure,χ, in terms of structural parameters that relate the phase and amplitude of EXAFS oscillations to the distance, type, and a number of backscattered atoms

around the central absorbing atom. The EXAFS function χ is typically plotted in terms of the photoelectron wave vector *k,* where *k* is related to kinetic energy of the photoelectron (*E*) by:

$$\kappa = [(\frac{2m}{h^2})(E\text{-}E_0)^{1/2}, \quad (1)$$

where, E_0 is the threshold energy of the photoelectron at $k = 0$, and m is the mass of the electron. A typical form of the EXAFS function for a single set of atoms *(N_j)* at a particular distance (R) is given by:

$$\chi(\kappa) = \sum_j N_j S_0^2 \left(\frac{F_j}{\kappa R^2}\right) \sin(2\kappa R + 2\delta^c + \phi) e^{-2\delta^2 k^2} e^{-2R\lambda}, \quad (2)$$

where, F_j is the effective curved-wave backscattering amplitude of the scatterer, δ^c and ϕ are phase shift for the absorber and backscatter, respectively, S_0^2 is a many-body amplitude reduction factor, δ^2 is a Debye-Waller term (or a mean-square relative displacement) assuming a harmonic oscillator, and χ is the mean free path of the electron. Quantitative extraction of R and N_j from experimental data requires that all of the terms affecting $\chi(k)$ must, in some way, be taken into account. This is accomplished by reference to a known structure for which the EXAFS function represented by equation 2 is either measured experimentally or calculated from ab initio theory.[3] The filtered experimental reference spectra are separated into two k-dependent functions, a total phase function that implicitly contains phase shifts for both the absorber ($2\delta^c$) and backscatter (ϕ) atoms and a total amplitude function containing the terms for F_j, S_0^2,and χ in equation (2). Nonlinear least-squares methods are used to fit the filtered unknown spectrum to a reference EXAFS spectrum of known *R* and N_j by varying R, N_j, and typically, δ^2 in equation 2, and E_0 in Equation (1). The structural parameters were obtained by nonlinear least squares fitting in k-space with a k3 weighting of the total experimental EXAFS spectra. The quality of the fit can be judged from the normalized sum of residuals.

$$r\ factor = \sum_n \left| k_n^3 \chi_{\exp t}(k_n) - k_n^3 \chi_{fit}(k_n) \right| / \sum_n \left| k_n^3 \chi_{\exp}(k_n) \right| x100 \quad (3)$$

Spurious peaks may thus occur in the modified radial distribution functions due to series termination errors. Estimated errors of 10 -20% occur in the determination of the number of first-shell neighbors.[4] These errors increase in the case of the determination of coordination numbers of higher shells, because additional effects may influence the amplitude of the corresponding EXAFS oscillation.

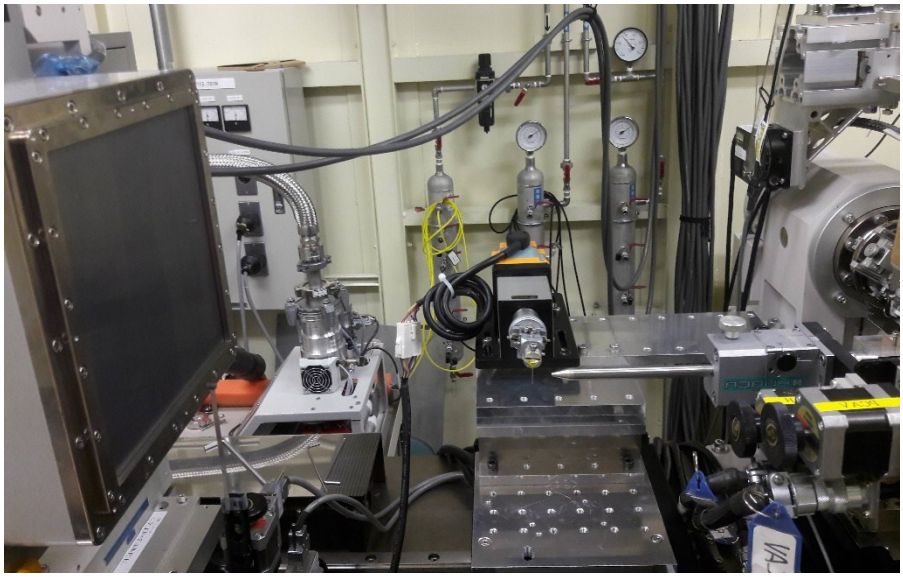

Fig. S4 Set up for Angle dispersive X-ray diffraction experiment

Supplementary results and discussion

As shown in Fig. S5a, UV pulse laser induced better crystallization of hybrid perovskites in acetonitrile solution. The *in-situ* ADXRD intensity indicated the stepwise crystallization, indicating Nanosecond pulsed laser irradiation of hybrid perovskites in solution can boost its crystallization and crystal growth. A few seconds of laser light irradiation are enough to trigger this crystallization. We further used this approach to treat thin film.

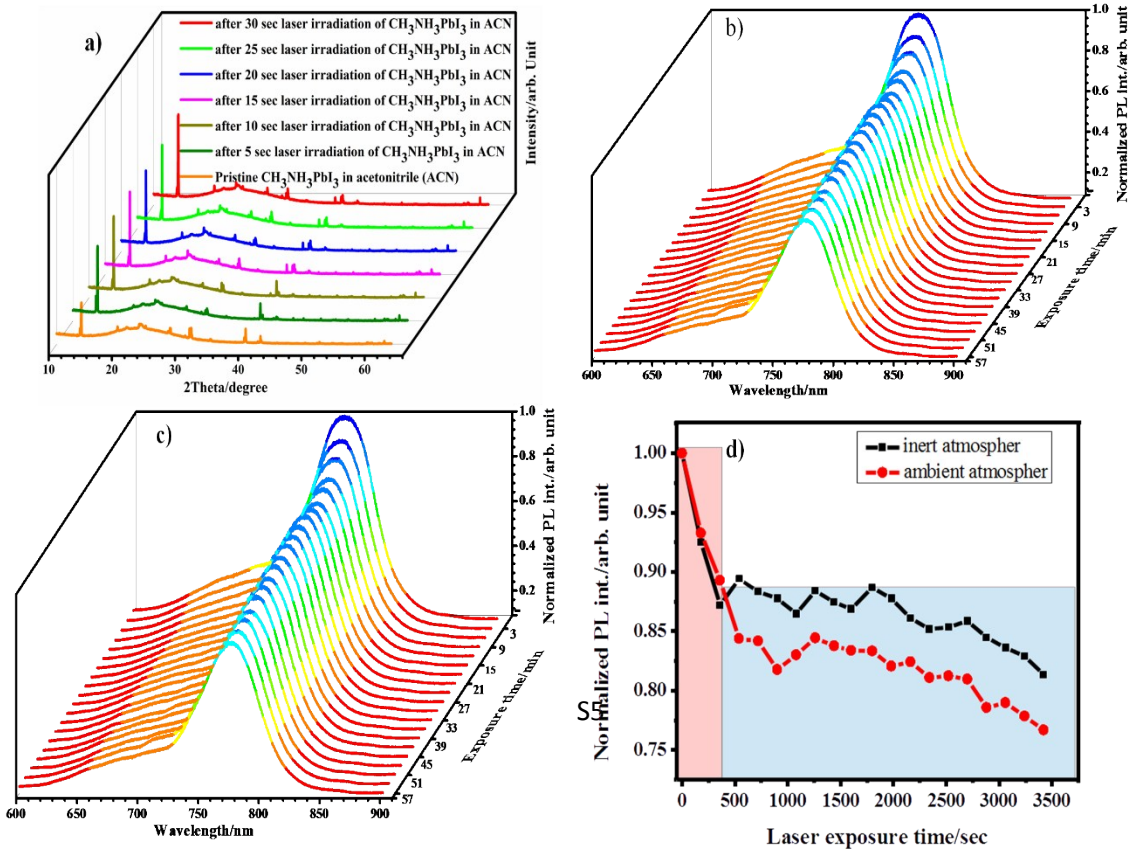

Fig. S5 Laser irradiation induced perovskite solution crystallization and photoexcited decay. (a) 532 nm laser irradiation induced perovskite crystallization in solution and Steady-state PL spectra of the $CH_3NH_3PbI_3$ film at continuous 266 nm laser irradiation of perovskite thin film. (b) Inert and (c) ambient atmosphere and, (d) PL intensity versus continuous laser irradiation time. Note that the power density for 266 nm lasers was power density of 10 mW/cm^2. Emission wavelength was at 765 nm.

According to the observations from the PL decay processes shown in Figs. S5a-5d, we performed *in-situ* Raman after extended irradiation of $CH_3NH_3PbI_3$ using the UV laser and find that the shape of the Raman spectra, obtained after steady-state PL measurement using 266 nm laser excitation were similar to those for $CH_3NH_3PbI_3$ irradiated with longer exposure times using a 532 nm laser (Fig. S6a). The spectra before and after laser irradiation are significantly different, indicating non-thermal phase transitions were taking place, due to the high photon flux. The decrease in FWHM of the main PL peak (low energy band) from 0.112 to 0.110 eV under nitrogen atmosphere and 0.111 to 0.109 eV under an ambient atmosphere, indicates less disorder, or a decrease in the degree of heterogeneity and more crystalline of the perovskite film's morphology after laser long exposure times. At room temperature, a 1.6 eV electronic bandgap has been reported using photoluminescence spectroscopy.[5] In addition, computational results,[6, 7] suggest that cubic $CH_3NH_3PbI_3$ has a smaller electronic bandgap compared to tetragonal and orthorhombic $CH_3NH_3PbI_3$. The red shift of electronic band gap position from 1.6 to 1.59 eV, decrease in FWHM from 0.112 to 0.110 eV and the intensity increase in the PL shoulder at 1.75 eV ((Fig. S6b)) are all associated with a phase transition to cubic $CH_3NH_3PbI_3$ and a decrease in the degree of heterogeneity. These changes are thought to be responsible for the slow decay of $CH_3NH_3PbI_3$. This is consistent with the longer phonon lifetime seen with Raman measurements and discussed in the next discussion and the slow PL decay process at longer exposure times from the steady-state PL measurements in Figs. S5b, S5c, and S5d. Motivated by these results, we combined PL with TRPL to study the photo-excited state dynamics and the interplay of disorder and morphology heterogeneity as well as laser-induced increase in crystallinity. In the nitrogen atmosphere, the carrier decay time of perovskite film, which is proportional to the PL intensity, becomes longer compared to that measured in ambient atmosphere during laser longer irradiation (Fig. S6). We assign those high energy peaks (at 1.75 eV) to band edge luminescence of the $CH_3NH_3PbI_3$, while we believe that shoulders shown in Fig. S6b and S6c are induced by the presence of the crystal disorder due to high volatility properties of iodine[8]. The splitting of the shoulder peak in the PL (at 1.75 eV) at longer exposure time in inert atmosphere indicates the distortion and breakdown of Pb-I bonding.

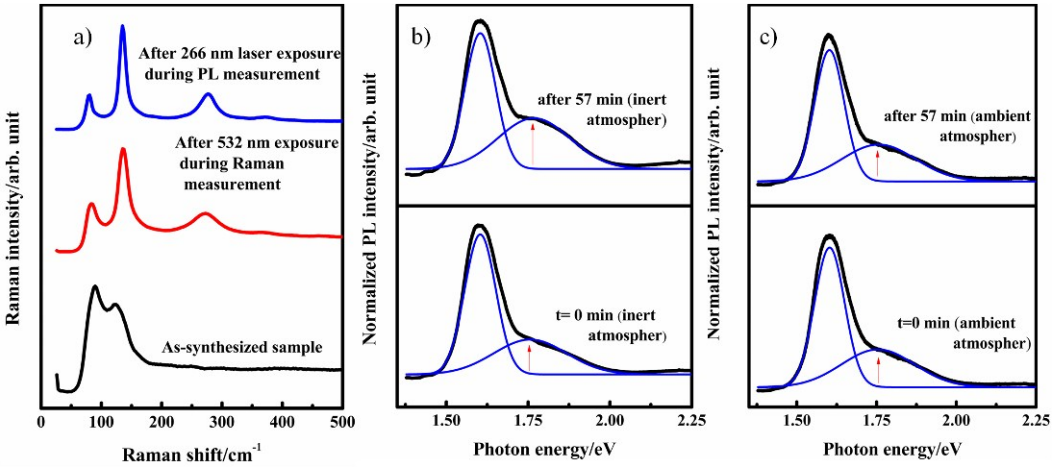

Fig. S6. (a) Raman and, (b) and (c) PL spectra of as-synthesized film and after 532 nm laser exposure in Raman (with 30% laser power) and 266 nm in PL measurements, with a power density of 10 mW/cm^2).

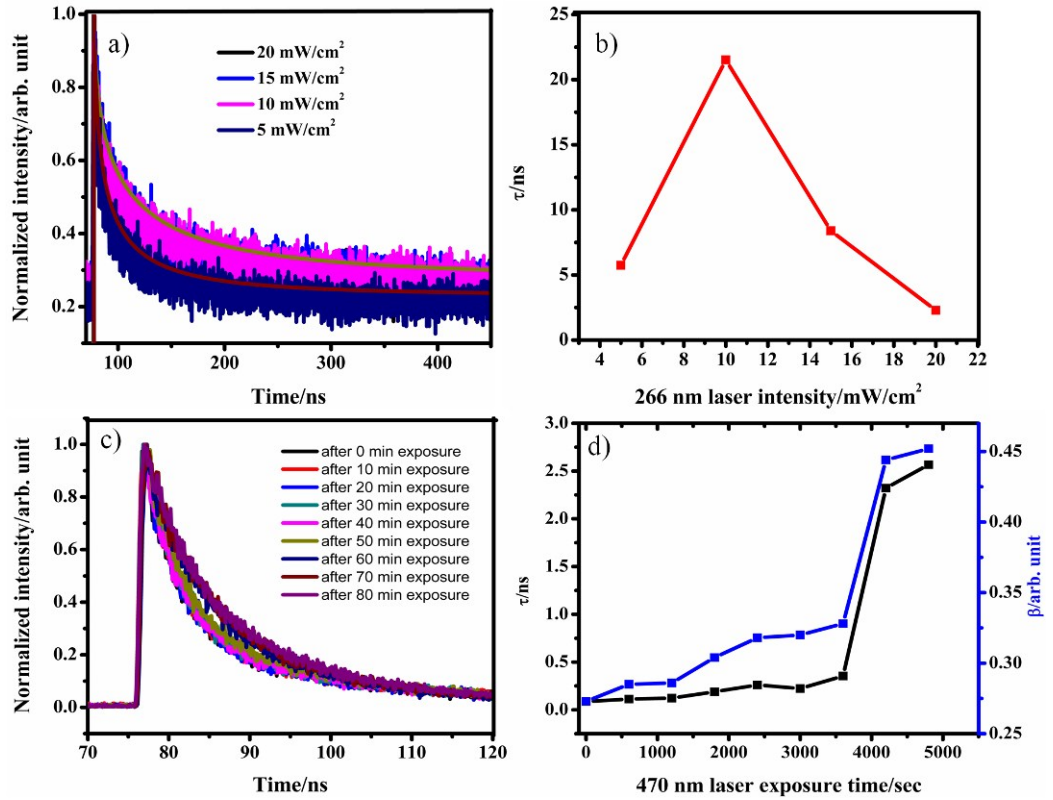

Fig. S7. Laser irradiation induced photoexcited carrier dynamics. (a) time-resolved PL after excitation of the $CH_3NH_3PbI_3$ film using 266 nm laser at different laser intensity, each irradiated for 8 min and (c) time-resolved PL after excitation using 470 nm laser at different exposure time, respectively. (b) Decay time versus laser intensity and (d) dynamics of the time-dependent decay time and β values fitted to a stretched exponential function.

Any increase of crystal defects will affect the electron lifetime, which translates to a decrease of the Raman intensity. These defects may act as a recombination center and mainly determine the lifetime. This is valid for Pb-I, I-I peaks and MA peak intensities as shown in Fig. 8. The intensity of these bonding signals are also directly proportional to the defects concentration and this needs further investigation. This gives raise to the similar behavior of the Raman peak intensities. In Stage 1, The intensity of these signals increases with an increase in defects concentration, for instance, native defects (V_I^+, MA_i^+, V_{MA}^-, and I_i^-).[9] We, therefore, expect these signals to be proportional to each other (Fig. S8). In Stage 2, the effect of the reduced electron lifetime dominates, so the integrated intensity of the peaks changes compared to stage 1. In Stage 3, upon further increasing the laser exposure time, the intensity increases and gradually decreases. The reduced electron lifetime in Stage 2 is recovered at this stage and this may be due to better quality of microstructure of the laser annealed cubic $CH_3NH_3PbI_3$ structure or defect depletion. Thus, one can observe that the integrated intensity of the peaks changed as compared to Stage 2. The gradual decrease in intensity could be due to a harmonic decay or further laser ablation of the thin film and consequently, the lifetime becomes gradually decreases. Furthermore, it is obvious that Raman spectral pattern attributes such as the number of peaks, peak positions, width, intensities and peak area are sensitive to species, structure, phase, and composition of minerals, and also to temperature and pressure.

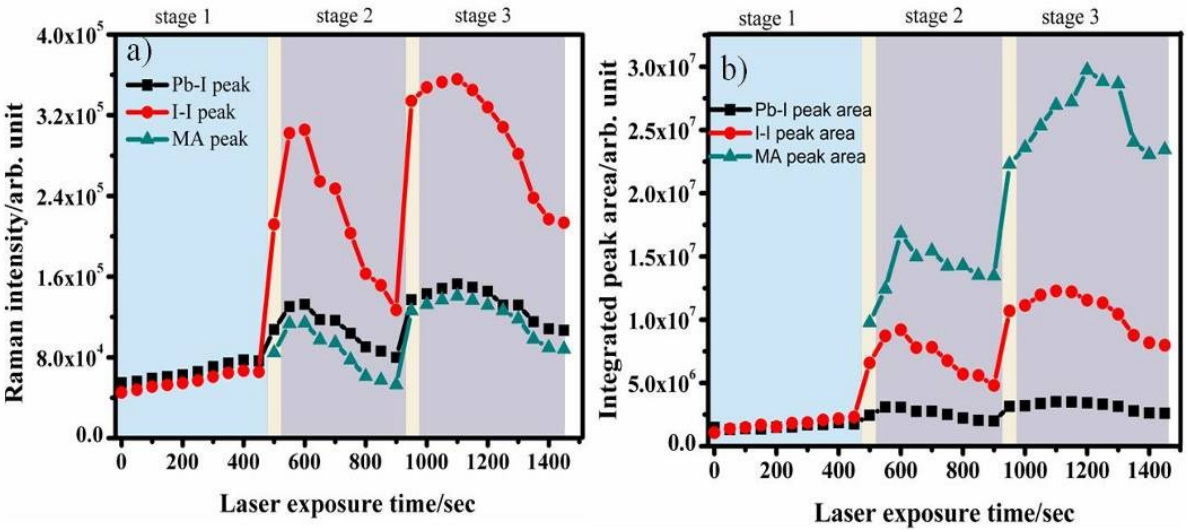

Fig. S8. Raman intensity and integrated peak area evolutions for the $CH_3NH_3PbI_3$ film. (a) Intensity and (b) integrated peak area evolutions with 532 nm laser irradiation time. All units are arbitrary. Note

that MA peak represents C-N bonding of methylammonium cation in the perovskite structure. Stages 1, 2 and 3 represent the range of time at which the integrated Raman intensity changes.

In addition to the peak intensity, peak positions and widths of the inorganic and organic cages reflect the degree of structural orders. Any deviation of peak position or width means a change in the degree of disorder in the microstructure. Fig. S9a shows both the width and peak position of the Raman peak of I-I lattice mode. The width of the I-I Raman band can be predictive of positional disordering in both tetragonal and cubic $CH_3NH_3PbI_3$ perovskites. The FWHM and peak position are correlated with the level of order inside the $CH_3NH_3PbI_3$ polycrystalline matrix. The structure of tetragonal $CH_3NH_3PbI_3$ has been determined experimentally to be body-centered tetragonal (space group I4cm)[10] with PbI_3^- octahedral tilted along the c-axis.[11] The octahedral on two adjacent layers tilt in opposite directions (out of phase). The $(CH_3NH_3)^+$ cations can freely rotate at room temperature,[6] which makes the body-centered tetragonal structure possible. At Stage 1 of Fig. S9a, the higher the width and the lower the peak position indicates the presence of disorder in the PbI_3^- octahedron of tetragonal $CH_3NH_3PbI_3$. The inverse correlation between the width and position of the Raman peak is clearly shown in Figs. S9a and S9b. These oscillations are due to structural transformations between metastable states which have different degrees of disorder. The oscillatory structural changes indicated by the zigzag FWHM at Stage 1 of Figs. S9a and S9b may reason from the forward and backward transitions of atoms between metastable states separated by energy barriers $E > KT$.[12] The large thermal fluctuations of the hopping atoms are assisted by the transient electron trapping of the photogenerated electrons.[13, 14] This zigzag or hopping of FWHM may be a suggestive behavior for the tetragonal structure as shown in Fig. S9a, at stage 1. In Stage 2 of Fig. S9a and S9b, the system is clamped to the more crystalline state and cannot show the quasi-periodic like oscillations. It can be seen that the FWHM of iodine lattice mode become smaller; the peak position goes to the higher wavenumber compared to FWHM and peak position of the iodine-iodine lattice in Stage 1. This implies that the PbI_3^- cage in cubic $CH_3NH_3PbI_3$ is more ordered than in tetragonal $CH_3NH_3PbI_3$. In addition, the up shift of the Raman shift and the narrowing of the line width as seen in Fig. S9c imply the breaking of the electron-phonon coupling. This is consistent with the results published by Weller et al. about the temperature dependent atomic migration within perovskite framework.[15] The Stage 2 of Fig. S9c shows the degree of disorder on the perovskite cubic scaffold. When the disorder increased the Raman width for the organic cage strongly increased compared to the inorganic cage in Stage 2. In this stage, the decrease in intensity of MA peaks compensated by the increase in FWHM. The FWHM of the MA peak in the Raman band can be predictive of orientational disordering in cubic $CH_3NH_3PbI_3$ crystal with relatively small contribution

from atomic disordering of I-I. In cubic $CH_3NH_3PbI_3$, the methylammonium cation becomes orientationally disordered at the unit cell center primarily along the three unit cell directions with a weak hydrogen bond between N-H and I^- interactions at 3.12(2) Å and 3.52(2) Å.[15] In Stage 2 of Fig. S9b, the higher FWHM indicates more disorder present in the methylammonium, while a smaller FWHM indicated more order present in the PbI_3^- framework. Due to the significant increase in FWHM for the organic Raman band, more short-range order presents in cubic $CH_3NH_3PbI_3$. Note that the high structural disorder is directly responsible for very broad bands and larger FWHM.[16] In Stage 3, the decrease in the FWHM of all Raman bands is compensated by the intensity of Pb-I, I-I, and MA, and therefore the FWHM in this stage is smaller compared to that shown in Stage 2. Narrowing the Raman bands is an implication to high structural order in cubic $CH_3NH_3PbI_3$ and more organized microcrystalline structure of cubic $CH_3NH_3PbI_3$ may be caused by the laser-induced thermal annealing. The increase in electron lifetime was interpreted as the increase of the intensity of Pb-I, I-I, and MA in this stage. Such defect removal or vacancy annihilation can be responsible for the recovery of the Raman spectral profile in Stage 3. Thus, the electron-phonon coupling can be reversibly controlled by the generation and annihilation of specific defects due to laser irradiation and thermal annealing.[17] Therefore, the microstructure evolution induced by photo-thermal effects led to significant changes in the strength of electron-phonon interactions. It can be concluded that the PbI_3^- octahedron has displasive character, while the methylammonium ion has the order-disordered character.

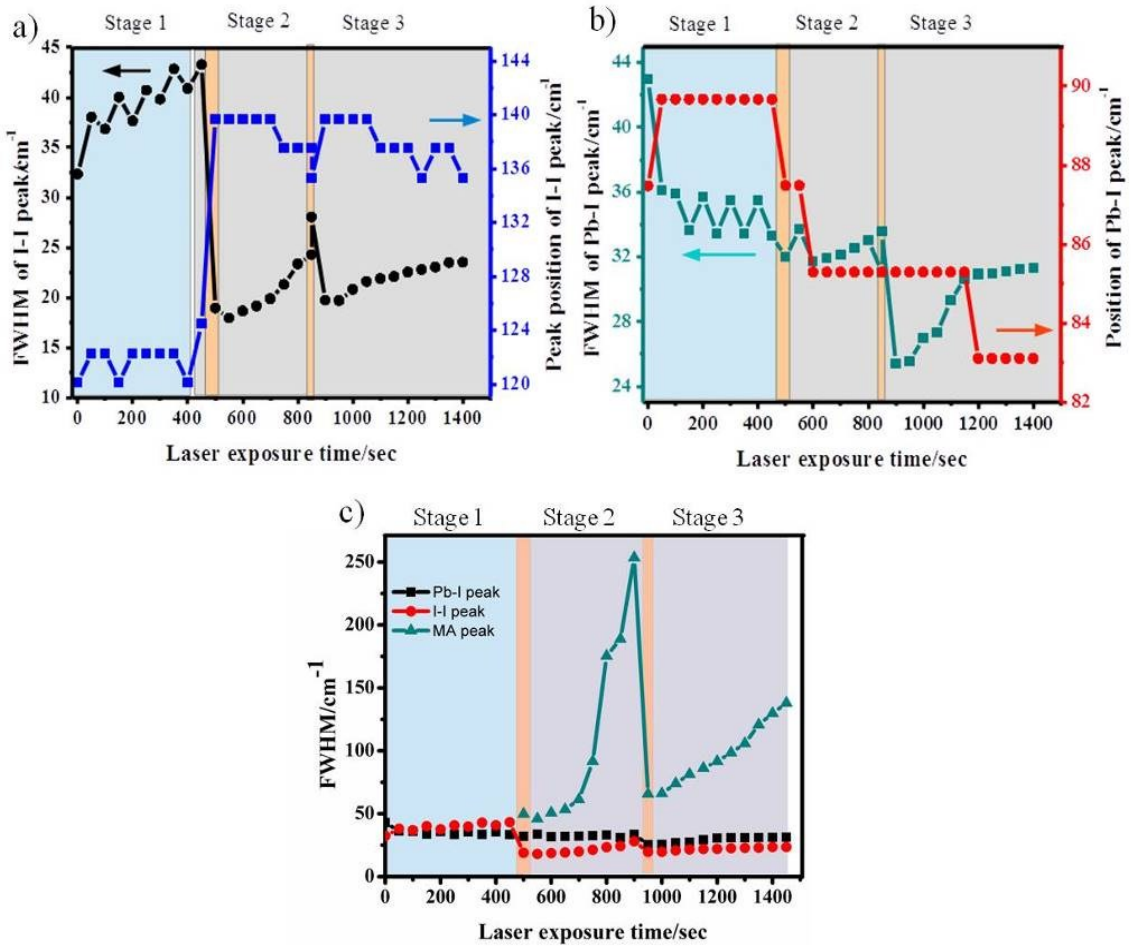

Fig. S9. Raman peak position and width change with longer laser irradiations time. Raman peak position shift of (a) Pb-I and (b) I-I signals corresponding to the distortion of PbI_3^-octahedron. (c) FWHM for the $CH_3NH_3PbI_3$ film under 532 nm with 30% laser power exposure.

Table S1. Raman peak intensity ratio representing structural distortion and formation of sharp and more intense Raman peak of $CH_3NH_3PbI_3$ thin film using 532 nm and 30% laser power.

Laser exposure time /sec	Raman peak intensity ratio ($I_{Pb\text{-}I}/I_{I\text{-}I}$) /arb. Unit
0	0.82
50	0.85
100	0.87
150	0.88
200	0.89
250	0.88
300	0.87
350	0.88
400	0.87
450	0.87
500	1.96

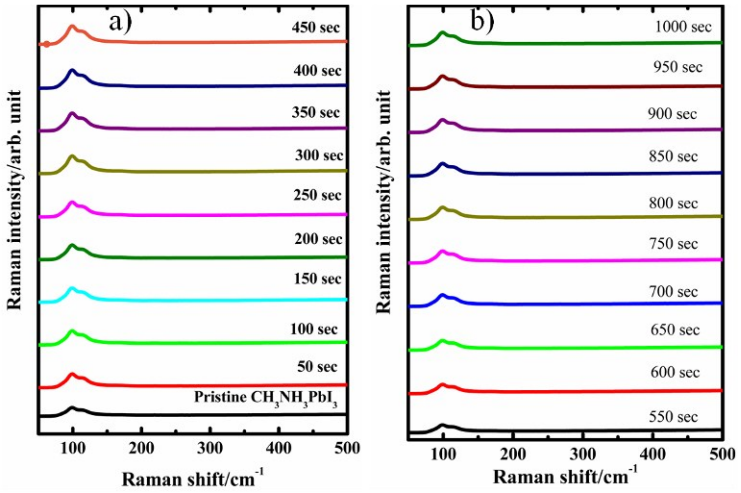

Fig. S10. Raman spectra with 632.8 nm laser irradiation of the $CH_3NH_3PbI_3$ films at different irradiation time with 30% laser power exposure.

As shown in Fig. S11a, the temperature induced changes started at 40 °C. The X-ray diffraction peak at 13.89° disappeared and then peaks at 28.1, 31.6, 40.6 and 42.6° disappeared during the phase transition temperature, 57.7 °C. But the peak at 23.4° continued up to 57 °C. Finally, the peaks obtain at 100 °C shifts to lower 2Theta values indicating the formation of new phase, cubic, at 14.0, 28.22, 31.65, 34.77, 40.36 and 42.94°. The temperature induced evolution of micro-Raman peaks followed

similar evolution pattern with the X-ray diffraction patterns. Raman spectra with a new broad peak at 300 cm^{-1} appear at 100 °C (Figure S11b). This new Raman pattern verified the formation of cubic phase. From both XRD and micro-Raman structural evolution, we can understand the presence of two phases (competition between the disappearance of the tetragonal and appearance of the cubic phase or coexistence of two phases) indicating the structural heterogeneity and distortion.

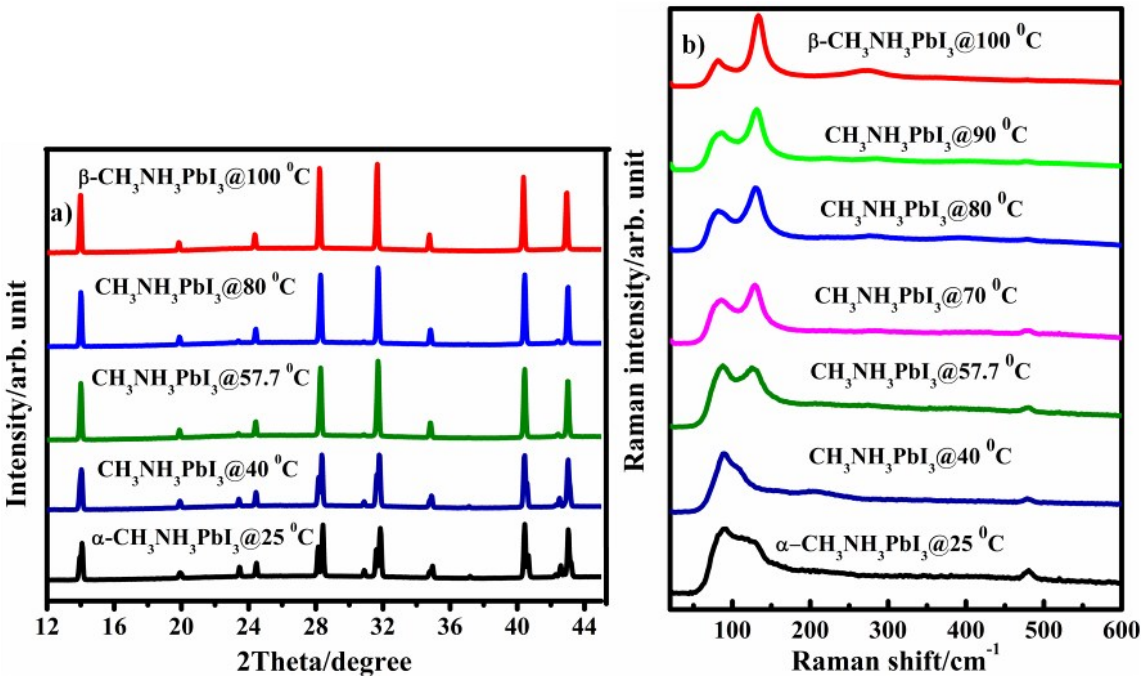

Fig. S11. Temperature-induced structure and microstructure evolution of $CH_3NH_3PbI_3$. a) *In-situ* synchrotron-based X-ray diffraction and b) *In-situ* micro Raman study at 25 - 100 °C. The holding time for each data record is every 3 minutes.

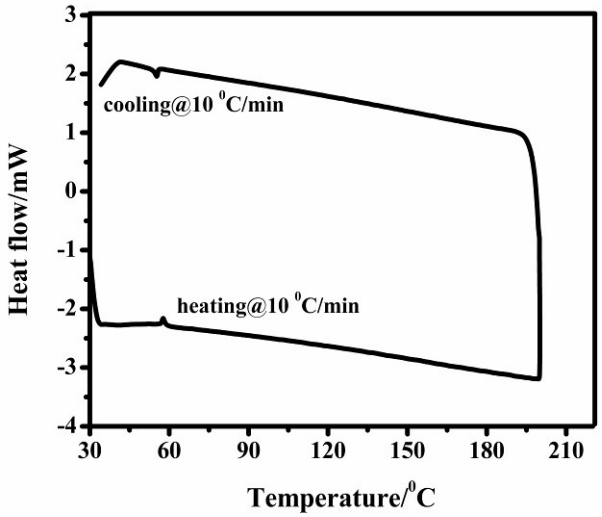

Fig. S12. Differential scanning calorimetry study of perovskite powder under the heating-cooling circle.

Phonon lifetime study: Raman spectroscopy is one of the most effective and important approaches to study phonon lifetimes. The energy-time uncertainty relation for the determination of phonon lifetime is given by Equation (4):[18]

$$1/\tau_{ph} = \Delta E/\hbar = 2\pi c\Gamma \qquad (4)$$

where, τ_{ph} is phonon lifetime, ΔE is the uncertainty in the energy of phonon mode, $\hbar$ is the reduced plank constant, Γ is full width half maximum (FWHM) expressed as cm^{-1}. The calculated phonon lifetime pattern is shown in Fig. S13. Initially, the phonon lifetime was small with values increasing as the sample transformed from α-$CH_3NH_3PbI_3$ (tetragonal phase) to β-$CH_3NH_3PbI_3$ (cubic phase). Since the amount of defects in tetragonal $CH_3NH_3PbI_3$ is very high, the confined phonon may undergo elastic and inelastic scattering process with crystal defects limiting the phonon lifetime. As laser exposure time increased, the phonon density may increase, and the inharmonic phonon coupling may also increase due to the longer time laser exposure inducing local heating, which finally increased the decay time, or the lifetime, of the phonons,[19] suggesting that $CH_3NH_3PbI_3$ is a promising absorber for future hot carrier solar cells (HCSC)[20] as indicated by the direct *in-situ* transformation of the low symmetry tetragonal structure to high symmetry cubic structured $CH_3NH_3PbI_3$ absorber material which restricts Ridley loss through narrow optical dispersion.[21] In HCSC, deriving the phonon population out of equilibrium can help keep the carrier populations hot, and thus increase the solar cell's efficiency.[22, 23] Long-lifetime phonons can be reabsorbed by electrons in HCSC,[24] to return energy to the electrons that would otherwise have been lost as heat, thereby improving efficiencies in photovoltaic[24] and laser devices.[25] However, phonon reabsorption by carriers degrades the efficiency of some devices e.g. light-emitting diodes (LEDs).[26] Phonon lifetime is also a key determinant of

carrier relaxation processes in semiconductors and ultrafast optoelectronic devices.[18] Finally, it is important to point out that the picoseconds phonon lifetime indicates wide range application of $CH_3NH_3PbI_3$ in laser, LEDs, solar cells and ultrafast optoelectronic devices.

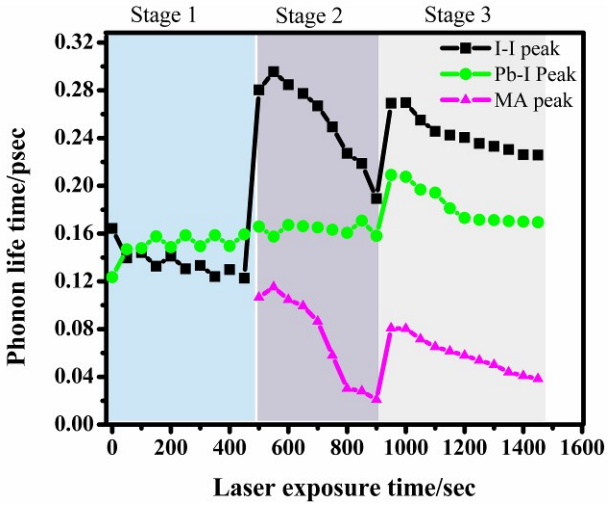

Fig. S13. Variation of phonon lifetime of perovskite sample under laser irradiation.

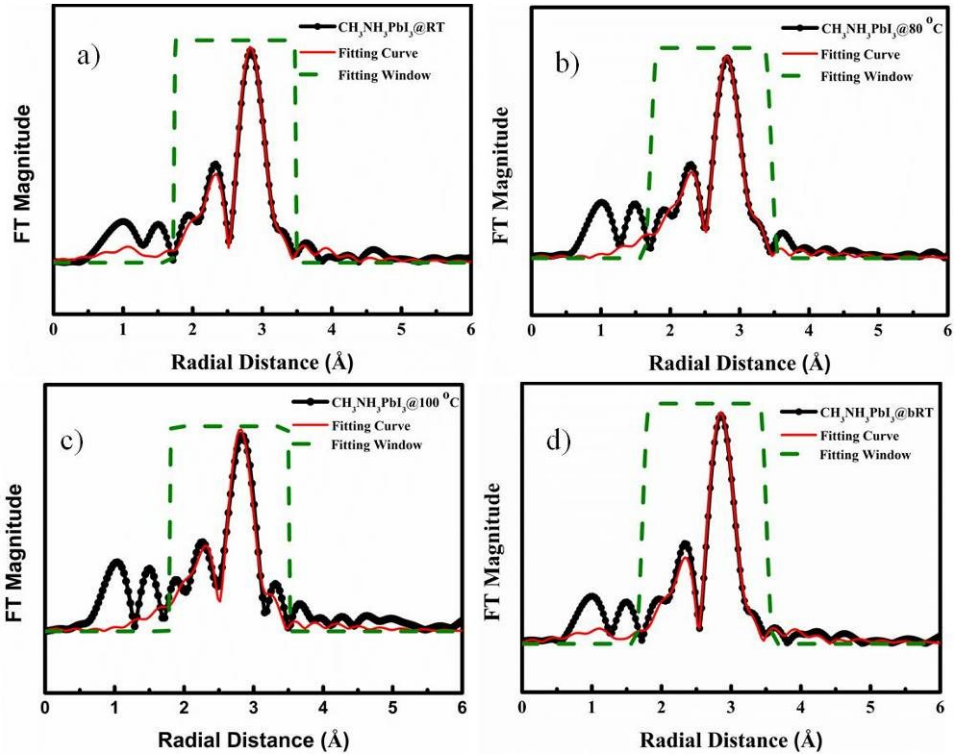

Fig S14. χ(R) spectrum of the Pb L_3-edge for the $CH_3NH_3PbI_3$ powder sample. The Fourier transform window and corresponding fitted results in the green dashed line and the red line are fitting curves.

Table S2 Structural parameters of $CH_3NH_3PbI_3$ obtained from EXAFS spectra

Sample	Shell	N	R (Å)	σ (Å^2) *10^{-3}	r-factor	Note
$CH_3NH_3PbI_3$	Pb-I(1)	4	3.211 +/- 0.013	19.78 +/- 2.34	0.004	Tetra.
Pb-I(2)		2	3.095 +/- 0.014	10.05 +/- 1.05		
Laser 2 min	Pb-I(1)	4	3.201 +/- 0.014	18.83 +/- 1.65	0.007	Tetra.
Pb-I(2)		2	3.102 +/- 0.019	10.01 +/- 1.22		
Laser 4 min	Pb-I(1)	4	3.207 +/- 0.033	16.97 +/- 2.81	0.008	Tetra.
Pb-I(2)		2	3.105 +/- 0.026	9.95 +/- 1.41		
Laser 6 min	Pb-I(1)	4	3.209 +/- 0.026	15.01 +/- 2.32	0.008	Tetra.
Pb-I(2)		2	3.104 +/- 0.020	9.13 +/- 1.19		
Laser 8 min	Pb-I(1)	4	3.216 +/- 0.023	14.84 +/- 0.93	0.005	Tetra
Pb-I(2)		2	3.103 +/- 0.015	7.72 +/- 0.70		
Laser 10 min	Pb-I(1)	4	3.214 +/- 0.007	14.80 +/- 0.99	0.007	Tetra
Pb-I(2)		2	3.103 +/- 0.015	7.65 +/- 0.88		
Laser 12 min	Pb-I(1)	4	3.214 +/- 0.012	12.92 +/- 1.18	0.013	Tetra
Pb-I(2)		2	3.102 +/- 0.008	7.27 +/- 1.08		

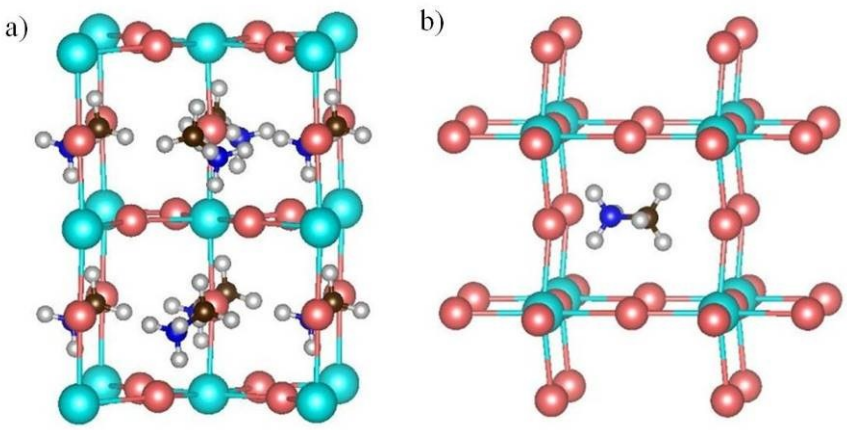

Fig. S15. Models of calculated crystal structures of the $CH_3NH_3PbI_3$ crystal showing Pb atomic local environment. Data calculated from x-ray absorption spectroscopy measurement at (a) 25 °C and (b) 100 °C.

Table S3. Structural parameters for calculated tetragonal $CH_3NH_3PbI_3$ model

Atom	Site	x	y	z
Pb	4*c*	0	0	0
I_{1-1}	4*a*	0.0092	0.0183	-0.2484
I_{1-2}	4*a*	0.0050	0.0139	0.2531
I_{2-1}	8*h*	-0.1710	0.3266	-0.0034
I_{2-2}	8*h*	0.1960	-0.3078	0.0069
I_{2-3}	8*h*	0.3240	0.1853	0.0010
I_{2-4}	8*h*	-0.3131	-0.1794	0.0058
N	16*l*	0.4191	-0.0802	0.2099
C	16*l*	-0.4679	0.0281	0.2597

Table S4. Structural parameters for calculated cubic $CH_3NH_3PbI_3$ model

Atom	Site	x	y	z
Pb	1*a*	0	0	0
I_1	12*h*	-0.0215	0.0002	-0.5020
I_2	12*h*	-0.0375	-0.5002	-0.9574
I_3	12*h*	0.4905	0.0000	-0.0530
N	12*j*	0.4513	0.4999	-0.5235
C	12*j*	-0.3314	-0.4999	-0.4308

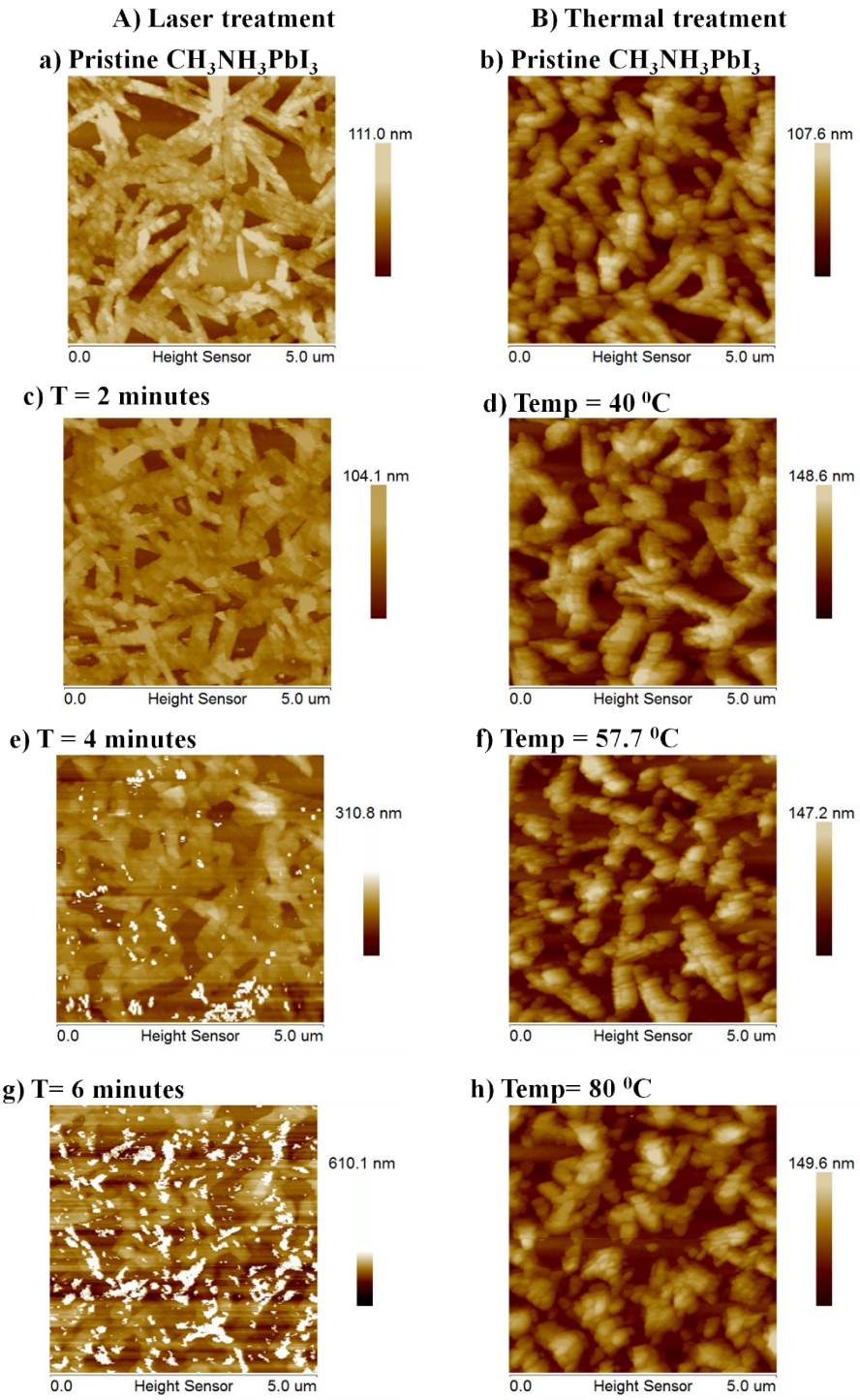

Fig. S16. In-situ morphology study of perovskite films under laser irradiation. AFM images of samples show the comparison of the (A) laser and (B) temperature induced the degree of morphological disorder and heterogeneity.

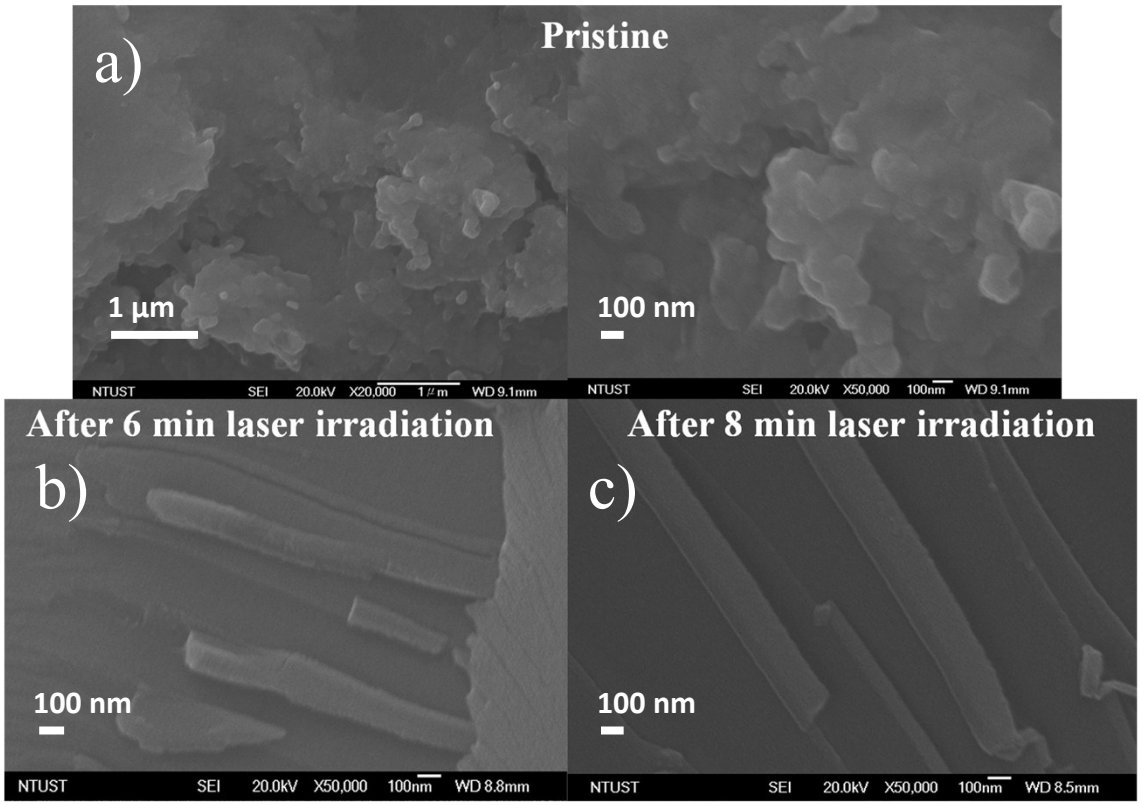

Fig. S17 Ex-situ morphology study of perovskite films under homemade 532 nm laser light irradiation. SEM images of a) pristine samples at 20000x and 50000x magnifications, b) after 6 minute and c) after 8 minute both b and c at 50000x magnifications. Note that the sample substrate over it perovskites was spin coated was cut into two pieces and then one was used as pristine without laser irradiations and the second one was used after irradiated with laser light. After irradiation the sample become smooth and 1D morphology was grown. This was done to avoid sample preparation differences induced unnecessary differences**.**

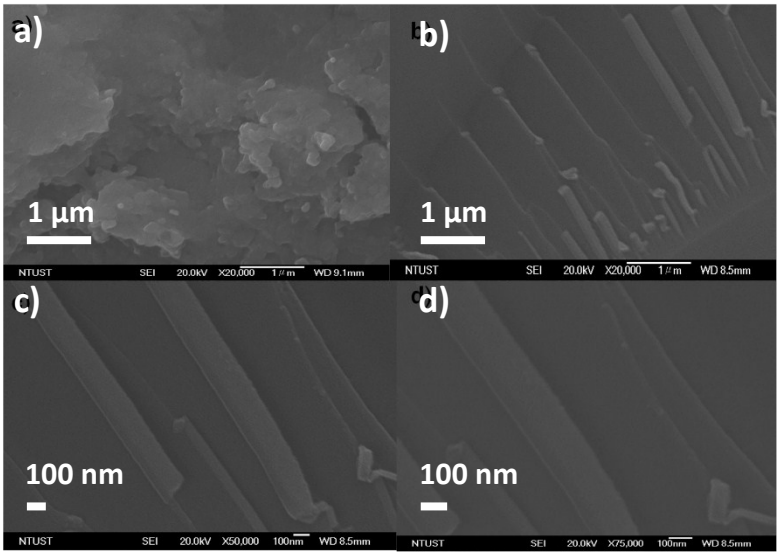

Fig. S18 Ex-situ morphology study of perovskite films under home-made 532 nm laser light irradiation. SEM images of a) pristine samples at a) 20, 000x and after laser irradiation for 8 minutes: b) 20, 000x, c) 50,000x and d) 75, 000x magnifications for the same sample coated on a glass slide substrate.

References

1. D. E. Sayers, *http://ixs.iit.edu/ subcommittee_reports/sc/sc00report.pdf*, 2000.
2. B. Ravel and M. Newville, *Journal of Synchrotron Radiation*, 2005, **12**, 537-541.
3. t. J. J. R. P.A. O'Day, i S.I. Zabinsky,t and C.E. Brown, Jr.t, *J. Am. Chem. SOC.*, 1994, **116**, 2938-2949.
4. I. Ojanperä, *TrAC Trends in Analytical Chemistry*, 1992, **11**, 222.
5. Y. Yasuhiro, N. Toru, E. Masaru, W. Atsushi and K. Yoshihiko, *Appl. Phys. Express*, 2014, **7**, 032302.
6. T. Baikie, Y. Fang, J. M. Kadro, M. Schreyer, F. Wei, S. G. Mhaisalkar, M. Graetzel and T. J. White, *Journal of Materials Chemistry A*, 2013, **1**, 5628-5641.
7. Y. Wang, T. Gould, J. F. Dobson, H. Zhang, H. Yang, X. Yao and H. Zhao, *Phys. Chem. Chem. Phys.*, 2014, **16**, 1424-1429.
8. V. A. Bibik and N. A. Davydova, *physica status solidi (a)*, 1991, **126**, K191-K196.
9. D. Yang, W. Ming, H. Shi, L. Zhang and M.-H. Du, *Chem. Mater.*, 2016, **28**, 4349-4357.
10. C. C. Stoumpos, C. D. Malliakas and M. G. Kanatzidis, *Inorg. Chem.*, 2013, **52**, 9019-9038.
11. M. H. Du, *J. Mater. Chem. A*, 2014, **2**, 9091-9098.
12. I. Abdulhalim, R. Beserman and Y. L. Khait, *J. Non-Cryst. Solids*, 1987, **97**, 387-390.
13. Y. L. Khait, *Phys. Rep.*, 1983, **99**, 237-340.
14. J. B. Pendry, P. D. Kirkman and E. Castano, *Physical Review Letters*, 1986, **57**, 2983-2986.
15. M. T. Weller, O. J. Weber, P. F. Henry, A. M. Di Pumpo and T. C. Hansen, *Chem. Commun. (Cambridge, U. K.)*, 2015, **51**, 4180-4183.
16. L. G. Cançado, A. Jorio and M. A. Pimenta, *Phys. Rev. B*, 2007, **76**, 064304-064307.
17. D. M. Edoardo Mosconi, Henry J. Snaith, Samuel D. Stranks and Filippo De Angelis, *Energy Environ. Sci.*, 2016, DOI: DOI: 10.1039/C6EE01504B.
18. N. Domènech-Amador, R. Cuscó, L. Artús, T. Stoica and R. Calarco, *Nanotechnology*, 2012, **23**, 085702.
19. E. Tea, H. Hamzeh and F. Aniel, *J. Appl. Phys.*, 2011, **110**, 113108.
20. M. B. Price, J. Butkus, T. C. Jellicoe, A. Sadhanala, A. Briane, J. E. Halpert, K. Broch, J. M. Hodgkiss, R. H. Friend and F. Deschler, *Nat Commun*, 2015, **6**.
21. G. Conibeer, S. Shrestha, S. Huang, R. Patterson, H. Xia, Y. Feng, P. Zhang, N. Gupta, M. Tayebjee, S. Smyth, Y. Liao, Z. Zhang, S. Chung, S. Lin, P. Wang and X. Dai, Hot carrier solar cell absorbers: materials, mechanisms and nanostructures, 2014.
22. G. Conibeer, R. Patterson, L. Huang, J.-F. Guillemoles, D. Kőnig, S. Shrestha and M. A. Green, *Sol. Energy Mater. Sol. Cells*, 2010, **94**, 1516-1521.
23. B. B. Varga, *Phys. Rev.*, 1965, **137**, A1896-A1902.
24. R. T. Ross and A. J. Nozik, *J. Appl. Phys.*, 1982, **53**, 3813-3818.
25. M. A. Stroscio, *J. Appl. Phys.*, 1996, **80**, 6864-6867.
26. S. Barman and G. P. Srivastava, *Phys. Rev. B*, 2004, **69**, 235208.